g-C$_3$N$_4$/CeO$_2$ Binary Composite Prepared and Its Application in Automobile Exhaust Degradation

Shengchao Cui [1], Baowen Xie [1], Rui Li [1], Jianzhong Pei [1,*], Yefei Tian [2], Jiupeng Zhang [1] and Xiangyang Xing [1]

[1] Highway school, Chang'an University, Xi'an 710064, China; cuishengchao@chd.edu.cn (S.C.); xiebaowen@chd.edu.cn (B.X.); lirui@chd.edu.cn (R.L.); zhjiupeng@163.com (J.Z.); xiangyang.xing@chd.edu.cn (X.X.)
[2] School of Materials, Chang'an University, Xi'an 710064, China; yftian@chd.edu.cn
* Correspondence: peijianzhong@126.com

check for updates

Abstract: Vehicle exhaust seriously pollutes urban air and harms human health. Photocatalytic technology can effectively degrade automobile exhaust. This work prepared g-C$_3$N$_4$/CeO$_2$ photocatalytic material by constructing heterojunctions. Four kinds of g-C$_3$N$_4$/CeO$_2$ composite photocatalytic materials with different mass ratios were prepared. An indoor exhaust gas purification test was carried out under natural light and ultraviolet light irradiations. The optimum mass ratio of g-C$_3$N$_4$ material and CeO$_2$ material was determined by evaluating the exhaust gas degradation effective. Moreover, the structure and morphology of the g-C$_3$N$_4$/CeO$_2$ composite were investigated with microscopic characterization experiments (including XRD, TG-DSC, FT-IR, UV-Vis, SEM and XPS). The results obtained were that the optimum mass ratio of g-C$_3$N$_4$ material to CeO$_2$ material was 0.75. The degradation efficiencies under ultraviolet irradiation in 60 min for HC, CO, CO$_2$, NO$_X$ were 7.59%, 12.10%, 8.25% and 36.82%, respectively. Under visible light conditions, the degradation efficiency in 60 min for HC, CO, CO$_2$ and NO$_X$ were 15.88%, 16.22%, 10.45% and 40.58%, respectively. This work is useful for purifying automobile exhaust in the future.

Keywords: g-C$_3$N$_4$/CeO$_2$; exhaust gas; degradation efficiency; photocatalytic material; heterojunctions

1. Introduction

While the development of science and technology has created a lot of wealth for human society, it also consumes a lot of energy and emits a large amount of waste gas and water, thus causing serious environment pollution and endangering humans' health [1]. Automobiles are the main contributors to atmospheric pollutant emissions, with CO, NO$_X$ and PM emissions exceeding 90% and HC exceeding 80%. The main components contained in automobile exhaust are NO$_X$, HC, CO and CO$_2$. Nitrogen oxides can cause environmental problems such as acid rain and ozone depletion. Nitrogen oxides can also produce photochemical smog with HC. The most famous photochemical smog events are the London photochemical smog and Los Angeles photochemical smog events [2]. Carbon dioxide is a greenhouse gas that can raise the Earth's temperature. Severe environmental pollution is destroying our ecosystem, so it is a significant task to govern and protect the environment [3].

In the 1970s, Japanese scholars Honda and Fujishma first found the photolysis of water under the bias condition by using a single crystal TiO$_2$ photoelectrode [4], and they successfully decomposed water into H$_2$ and O$_2$. It was later found that the TiO$_2$ material irradiated by light could not only decompose water but also be used to degrade organic pollutants. TiO$_2$ material could deeply oxidize most of the toxic organic substances [5]. This major discovery attracted a large amount of scholars'

interests, and there have been many outcomes related TiO_2 material [6–12]. However, TiO_2 has a large forbidden band width (about 3.2 eV) and cannot absorb solar light efficiently. It can only absorb 4%–6% of the ultraviolet band energy in the solar spectrum. Though the modified TiO_2 catalytic material has a greater performance than that of pure TiO_2 material, the catalytic effect still cannot effectively break through. Therefore, it is very meaningful to find and study materials that can make full use of solar energy.

Graphite phase carbon nitride is a non-metallic semiconductor material with the advantages of non-toxicity, low cost, and easy preparation. It is widely used in the production of clean renewable energy and environmental pollution control technologies. Its forbidden band width is about 2.7 eV, which can directly use solar energy, thus attracting a lot of scholars' attention and research [13–18]. However, the photogenerated electron-hole pairs of $g-C_3N_4$ are easily complexed and have a small specific surface area, resulting in a low photocatalytic activity [19,20]. Therefore, the photocatalytic activity of $g-C_3N_4$ could be improved by modifying methods. Building heterojunction is a common method for photocatalysts. For example, the photocatalytic efficiency of $g-C_3N_4/BiVO_4$ heterojunction is almost 5.3 times higher than that of an individual $g-C_3N_4$ sample [21]. In addition, $WO_3/g-C_3N_4$ heterostructure nanocomposites were found to possess excellent photocatalytic activity for degrading methyl orange (MO) and tetracycline (TC) under visible light irradiation [22]. In this work, CeO_2 was introduced to improve the photocatalytic efficiency of $g-C_3N_4$.

The cerium oxide material is a good catalyst with good oxygen storage and redox properties. It is a cubic fluorite-type structure that is composed of a face centered cubic cation and an anion occupying the octahedral gap position [23]. In this structure, the cation of each cerium element coordinates with the eight nearest oxygen element anions, and each oxygen element anion coordinates with the four nearest cerium element cations [24]. CeO_2 has a variable metal ion pair (Ce^{3+}/Ce^{4+}) under different redox reaction atmospheres. This property makes the CeO_2 material have an excellent oxygen storage and release capacity [25–27]. Furthermore, CeO_2 has a valence band of 2.35 eV and a conduction band of −0.23 eV, and it can form a composite heterojunction with graphite phase carbon nitride. The heterojunction structure can promote the dissociation of excitons and improve the separation efficiency of the photo-generated carriers of the catalyst, thereby achieving the purpose of improving the activity of the catalyst [28].

However, few works have focused on $g-C_3N_4/CeO_2$ heterostructure nanocomposites. Therefore, this work prepared a $g-C_3N_4/CeO_2$ heterostructure composite photocatalytic material with different mass ratios. An exhaust gas degradation test was carried out to obtain the optimal mass ratio of $g-C_3N_4$ and CeO_2. Under the optimal preparation conditions, the exhaust gas degradation test was conducted in 60 min. Moreover XRD, TG-DSC, FT-IR, UV-Vis, SEM, and XPS were executed to verify the performance of the $g-C_3N_4/CeO_2$ material.

2. Experiment and Methods

2.1. Materials and Equipment

The raw materials and test equipment are shown in Tables 1 and 2, respectively.

Table 1. Test equipment.

Device Name	Model	Factory
Alumina crucible	Φ100 mL	Shanghai Kesheng Ceramics Co., Ltd. (Shanghai, China)
Electronic balance	FA2004B	Shanghai Jingke Tianmei Scientific Instrument Co., Ltd. (Shanghai, China)
Muffle furnace	100 mL	Shanghai Pudong Physical Optical Instrument Factory (Shanghai, China)
Planetary ball mill	450 rpm	Changsha Miqi Equipment Co., Ltd. (Changsha, China)
Magnetic stirrer	0–2400 r/min	Changzhou Deke Instrument Manufacturing Co., Ltd. (Changzhou, China)
Electric centrifuge	0–4000 rpm	Jintan District Xicheng Xinrui Instrument Factory (Changzhou, China)

Table 2. Test raw materials.

Reagent Name	Model	Factory
Dicyandiamide	AR	Tianjin Fuchen Chemical Reagent Factory (Tianjin, China)
Cerium Oxide	AR	Tianjin Kemiou Chemical Reagent Co., Ltd. (Tianjin, China)

AR refers to analytical purity.

2.2. Preparation

The steps for preparing g-C_3N_4/CeO_2 are as follows:

(1) g-C_3N_4 was prepared by dicyandiamide thermal polymerization at 600 °C.

(2) Three grams of g-C_3N_4 powders were weighed and dispersed it into a mixed solvent of 10 mL of deionized water and 40 mL of absolute ethanol. The mixed solution was stirred evenly and recorded as solution A. Then, 3 g of CeO_2 powders were weighed and added to solution A, stirred, and recorded as solution B.

(3) A magnetic stirrer was used to stir solution B for 2 h, and then solution B was put in an oven at 80 °C for 12 h. The block solid could be obtained. Then, it was ground into powder and placed in a ceramic crucible.

(4) The crucible was placed in a muffle furnace at a heating rate of 15 °C/min and heated to 500 °C for 4 h, and then it was cooled down to 450 °C for 12 h. The sample that was obtained after calcination and cooling was the g-C_3N_4/CeO_2 binary composite material.

(5) According to the above method, binary composite materials with 1:0.5, 1:0.75, 1:1 and 1:2 mass ratios of g-C_3N_4 to CeO_2 were prepared.

2.3. Indoor Exhaust Gas Purification Step and Evaluation Method

Purification efficiency (η) can be used to evaluate the purification effect of the prepared materials on the exhaust gas. The purification efficiency formula can be written as the follows:

$$\eta = \frac{C_0 - C_t}{C_0} \times 100\% \tag{1}$$

where η is the purification efficiency, C_0 is the initial exhaust concentration, and C_t is the exhaust concentration after t minutes.

Therefore, we proposed a method for indoor exhaust gas purification. The indoor test process was as follows:

(1) The g-C_3N_4/CeO_2 photocatalytic material was prepared by following the above steps, and 3 g of g-C_3N_4/CeO_2 were weighed and then spread evenly on clean A4 paper;

(2) The exhaust purification system was connected in sequence. The exhaust purification system in this work is shown in Figure 1. Firstly, the DTN220B-NO_2 portable nitrogen dioxide detector was put into the reaction box, and a small fan was turned on to keep gas flowing. Then, the photocatalytic material was put into the reaction box, which was closed tightly. Secondly, the reaction chamber was covered with a curtain to prevent light from entering. Then, the air inlet valve was opened, and the air outlet valve was closed. The engine was connected to the air inlet and injected exhaust gas into the reaction box.

(3) The NHA-506 (5G) car exhaust gas analyzer (Nanhua Instrument Co., Ltd., Foshan, China) was turned on. After injecting for a period of time, the automobile exhaust gas analyzer was used to test the concentration of various components in the exhaust gas. When a certain concentration was reached, the intake valve was closed and the gasoline engine was turned off. The UV or incandescent lamp was turned on and the test was started.

(4) The concentrations of NO, NO$_2$, CO, CO$_2$ and HC were recorded every 10 min. A total of 60 min and 7 groups of data were recorded.

Figure 1. The exhaust purification system [29].

2.4. Error Correction of Exhaust Gas Purification Test

Because the engine parameters of each car are different, the exhaust gas concentrations that are produced are also different. In this work, it was concluded that each component was in a certain range after a large number of repeated works. Through a large number of inflation tests, it could be found that the concentration range of HC was 340–400 ppm, CO was 4%–6%, CO$_2$ was 5%–9%, and NO$_X$ was 40–80 ppm. The principle of this tail gas purification experiment was to use a car tail gas analyzer to suck the tail gas out of the gas purification box for testing. The exhaust gas component purification efficiency was calculated according to the initial concentration and the concentration at any time by Formula (1). However, the reduction of the exhaust gas concentration in the purification tank was composed of two parts, one of which was purified by the photocatalytic material and the other of which was extracted by the test instrument. Therefore, the process of determining which part was taken out by the instrument and which part was purified by materials was the key to ensuring the accurate calculation of photocatalytic efficiency. This article adopted the correction method to solve the problem of system error. The specific method was to use a large amount of blank test data to determine the correction value, which was the so-called blank test. The blank sample test used an exhaust gas purification test system. First, a sample was placed in the system, then it was tested again according to the purification process, and the data were recorded. After a large number of repeated tests, a large amount of data were obtained. The exhaust gas purification test was recorded every 10 min, so the blank test data were also recorded every 10 min. In this way, it could better reflect how the purification efficiency changed every 10 min. After a large number of blank sample tests, the final data are shown in Table 3. As can be seen from the table, the concentration of each component was reduced every 10 min with the passage of time. This was because the concentration of the gas in the environment box was decreasing, which also caused the concentration of the same volume of gas to be drawn down.

Table 3. Exhaust gas purification system error correction table.

Exhaust Gas Composition	0–10 min	10–20 min	20–30 min	30–40 min	40–50 min	50–60 min
HC (ppm)	10	6	8	6	6	5
CO (%)	0.1	0.06	0.06	0.06	0.06	0.06
CO$_2$ (%)	0.1	0.1	0.1	0.1	0.08	0.08
NO$_X$ (ppm)	8	5	6	2	1	1

2.5. Analysis of Exhaust Gas Degradation Efficiency

According to the above experimental procedure in Section 2.3, the degradation efficiency of the g-C_3N_4/CeO_2 composite that was prepared at different mass ratios could be calculated. The optimum ratio of g-C_3N_4 to CeO_2 could be obtained. Moreover, the degradation efficiency of tail gas at the optimum ratio was further studied.

2.6. Microscopic Test

Studies have shown that CeO_2 has a good visible light absorption capability and can degrade organic pollutants. The photogenerated electron-hole pair of g-C_3N_4 is easy to recombine when coupled with its low quantum efficiency and low catalytic performance, which limits its scale application in the field of degradation tail gas. Therefore, according to the band principle, g-C_3N_4/CeO_2 composites were prepared. The newly formed composite material was a special heterojunction structure, and the structure and morphology of the composite material were studied by microscopic characterization methods such as XRD, FT-IR, UV-Vis, TG-DSC, SEM and XPS.

3. Results and Discussion

3.1. Degradation Principle of g-C_3N_4/CeO_2

Figure 2 shows the principle of purifying exhaust gas by the g-C_3N_4/CeO_2 composite material. The conduction band is the energy space formed by free electrons. The valence band usually refers to the highest energy band in a semiconductor or insulator that can be filled with electrons at 0 K. It can be seen from the Figure 2 that, due to the special relationship between the valence and conduction bands of the CeO_2 material and the g-C_3N_4 material, a composite heterojunction photocatalytic material was formed. If the photon energy was higher than that of the photocatalyst absorption threshold when the sunlight irradiated g-C_3N_4/CeO_2, the valence band electron (e^-) of g-C_3N_4/CeO_2 occurred inter-band transition. When an electron transitioned from the valence band to the conduction band, a corresponding hole (h^+) was generated in the valence band. Then, a series of reactions occurred between the photo-generated electrons and the holes. For example, O_2 was adsorbed on the surface of g-C_3N_4/CeO_2 catalyst to form $\bullet O_2^-$ by catching electrons, and the generated holes could oxidize water on the surface of g-C_3N_4/CeO_2 to $\bullet OH$. $\bullet O_2^-$ and $\bullet OH$ were strong oxidizing groups that could oxidize most organic pollutants to CO_2 and H_2O. Since photogenerated electrons and holes were opposite charges, they would recombine through electrostatic forces, releasing or emitting energy to consume energy. The photo-generated carriers of g-C_3N_4 were easy to recombine. When the CeO_2 material was added, the photo-generated electrons could be transferred from the conduction band of g-C_3N_4 to the conduction band of CeO_2, and the photo-generated holes could be transferred from the valence band of CeO_2 to the g-C_3N_4 valence band. Therefore, the g-C_3N_4/CeO_2 photocatalytic material could effectively solve the problem of the low photo-generated carrier separation efficiency of the g-C_3N_4 material and could promote the dissociation of excitons, achieving the purpose of improving the photocatalytic activity of the g-C_3N_4 catalyst.
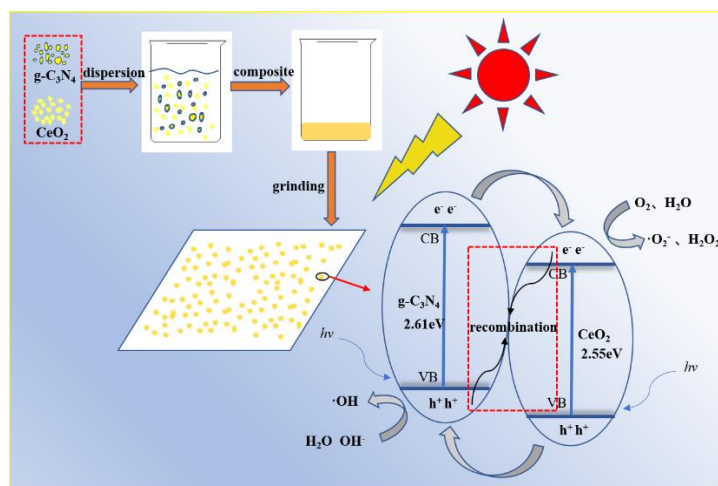
Figure 2. Principle of purifying exhaust gas with a g-C_3N_4/CeO_2 composite material.

3.2. Degradation Efficiency of g-C_3N_4/CeO_2

The degradation efficiencies of the binary composite that were obtained at different g-C_3N_4 to CeO_2 mass ratios was tested by the method described in Section 2.3. The photocatalytic purification effective after error compensation is shown in Figure 3.
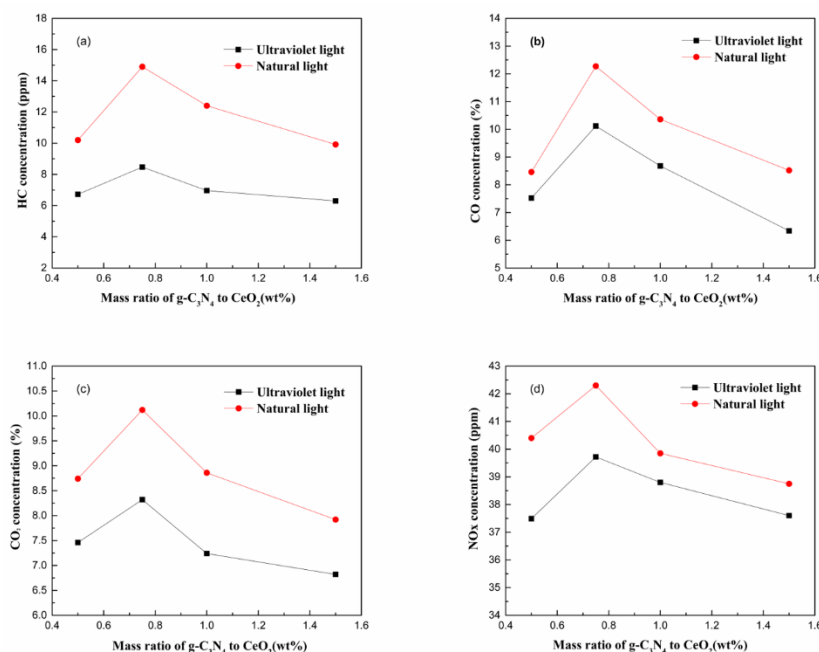

Figure 3. The purification effective change pattern at different g-C_3N_4 to CeO_2 mass ratios for (**a**) HC, (**b**) CO, (**c**) CO_2, and (**d**) NO_X.

It can be seen from the four graphs in Figure 3 that the degradation efficiency of exhaust gas under natural light conditions was better than that under ultraviolet light, and in both natural and ultraviolet light conditions, the degradation efficiency of the four components in the automobile exhaust had a peak. When the mixing mass ratio of g-C_3N_4 to CeO_2 was less than 0.75, the purification rate of each component increased continuously with the ratio increases. When the mixing mass ratio of g-C_3N_4 to CeO_2 was greater than 0.75, the purification rate of each component was continuously reduced with the ratio increases. From the above results, it could be concluded that the optimum blend ratio of g-C_3N_4 to CeO_2 was 0.75.

From the above analysis, when the mixing mass ratio of g-C_3N_4 to CeO_2 was 0.75, the binary composites had the highest purification efficiency for the four components in the exhaust gas under both natural light and ultraviolet light conditions. However, it could not indicate how the exhaust gas concentration changed every 10 min over 60 min. Therefore, when the mass ratio of g-C_3N_4 to CeO_2 was 0.75, the change trends of four components HC, CO, CO_2 and NO_X were studied. The results that were obtained are shown in Figure 4.
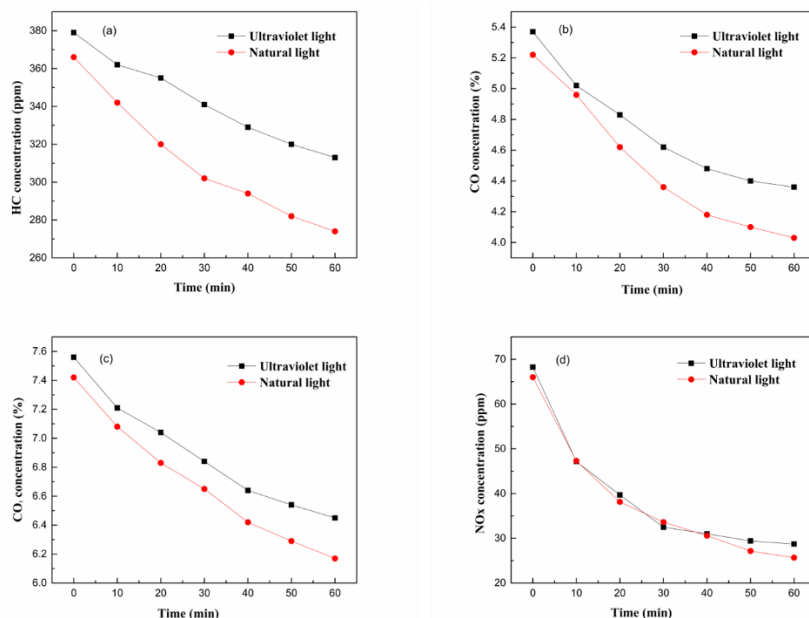
Figure 4. The change pattern of exhaust gas concentration (**a**) HC; (**b**) CO; (**c**) CO_2; and (**d**) NO_X.

It can be seen from Figure 4 that under ultraviolet light conditions, the degradation efficiencies of the g-C_3N_4/CeO_2 composites for HC, CO, CO_2 and NO_X in 60 min were 7.59%, 12.10%, 8.25% and 36.82%, respectively. Under visible light irradiation, the degradation efficiencies of HC, CO, CO_2 and NO_X in the 60 min were 15.88%, 16.22%, 10.45% and 40.58%, respectively. The trends of HC, CO, CO_2, and NO_X concentration patterns were concave curves, indicating that the degradation rate for exhaust gas in the initial stage was higher. With the extension of time, the purification and degradation rate of exhaust pollutants gradually decreased.

3.3. Micro Analysis

3.3.1. UV-Vis Analysis

Figure 5a shows UV-Vis DRS spectra of g-C_3N_4, CeO_2 and g-C_3N_4/CeO_2. All the samples showed an adsorption edge in the visible light region. The g-C_3N_4/CeO_2 material showed an adsorption edge of 550 nm, signifying its photocatalytic activity under visible-light irradiation and a significant blue-shift was observed for g-C_3N_4 and CeO_2 [30]. Based on the electronic absorption spectra, the band gap energy could be obtained [31]. The calculated band gap value of the samples is shown in Figure 5b. The band gaps of g-C_3N_4, CeO_2 and g-C_3N_4/CeO_2 were 2.61, 2.55, and 2.02 eV, respectively. The g-C_3N_4/CeO_2 binary composite showed a certain extent of red shift, corresponding to the high utilization of the visible light [32].

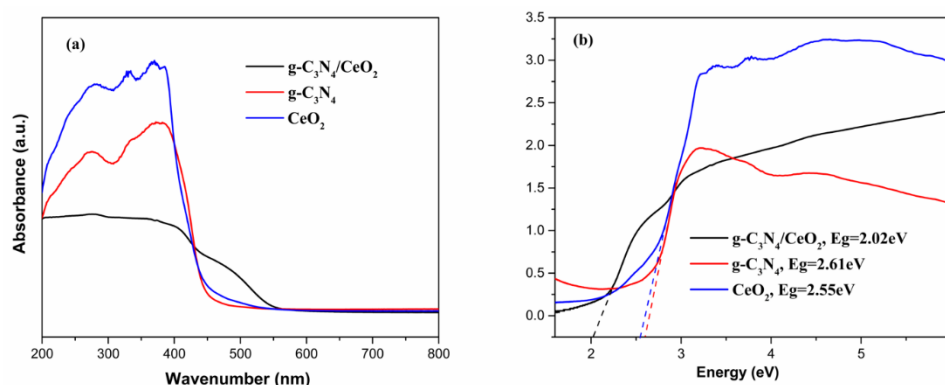**Figure 5.** (**a**) UV-Vis DRS, (**b**) plots of $(\alpha h v)^{1/2}$ vs. photon energy of g-C_3N_4, CeO_2, g-C_3N_4/CeO_2 samples.

3.3.2. FI-TR Analysis

Figure 6 shows the infrared vibrational spectrum of the prepared g-C_3N_4/CeO_2 binary composite at 2000–500 cm^{-1}. As can be seen from Figure 6, there was a significant difference in the infrared spectra between the two materials between 500 and 1300 cm^{-1}. Among them, the characteristic absorption peak in the range of 500–900 cm^{-1} was the stretching vibration absorption peak of Ce-O-Ce corresponding to the CeO_2 material. The characteristic absorption peak in the range of 1250–1725 cm^{-1} was the typical stretching vibration absorption of the C–N heterocyclic ring corresponding to the g-C_3N_4 material. It was a typical 3-s-triazine structure out-of-plane bending vibration peak at 1280 and 1458 cm^{-1}. This indicated that the sample was the binary composite of g-C_3N_4 and CeO_2. In other ranges, the infrared spectra of the two materials were similar, probably due to the lower specific gravity of the CeO_2 material, or possibly because the infrared absorption peak of the g-C_3N_4 material was stronger.
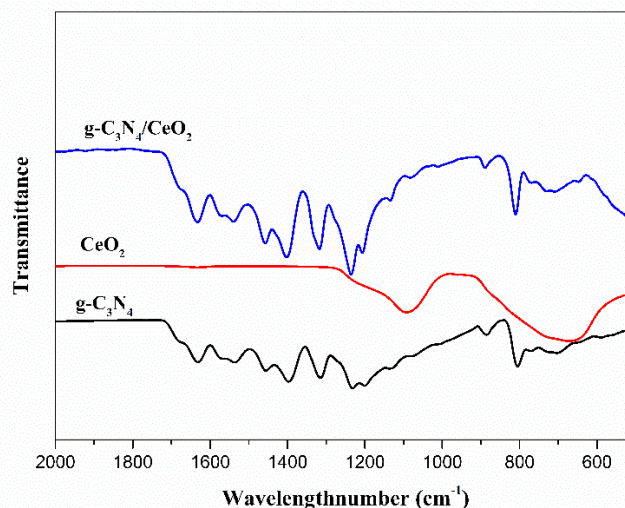

Figure 6. Infrared vibrational spectrum of the g-C_3N_4/CeO_2 binary composite.

3.3.3. XRD

Figure 7 is an XRD pattern of the g-C_3N_4/CeO_2 binary composite that was prepared by the optimum ratio obtained in Section 2.2. It can be seen from the figure that the peaks at the diffraction angles at 16.64° and 27.5° were characteristic peaks of g-C_3N_4. The diffraction peaks at 28.57°, 31.28°, 47.50°, 56.34°, 59.49°, 69.41°, 76.71° and 79.79° corresponded to the (111), (200), (220), (311), (222), (400), (331) and (420) crystal planes, respectively, of cubic fluorite-type CeO_2. They all corresponded to the standard JCPDS NO.34-0394 card of CeO_2 [23]. As can be seen from the figure, the mixed diffraction peaks of the two materials were relatively obvious, the peak width was narrow, and the crystallinity was good, so the prepared binary composite crystal form was better. Additionally, no other new crystal

phase was found in the prepared binary composite material, indicating that the obtained sample was a composite of the g-C_3N_4 and CeO_2 materials.

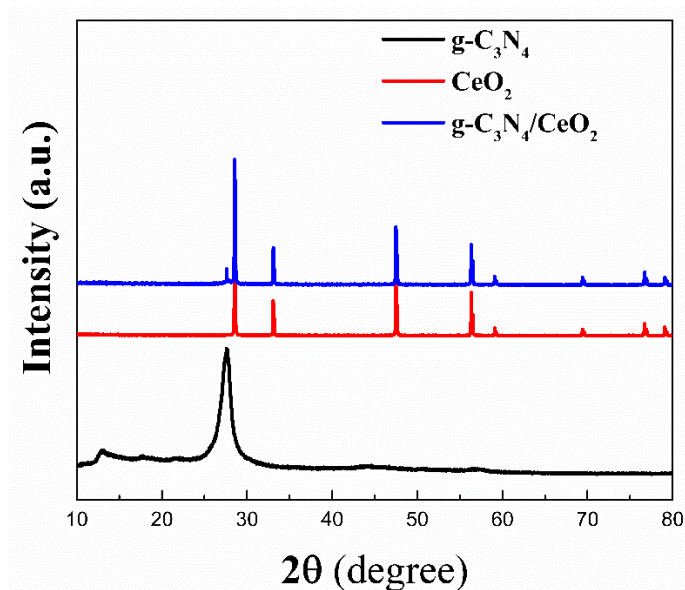**Figure 7.** XRD pattern of g-C_3N_4/CeO_2.

3.3.4. TG-DSC

Figure 8a is a TG-DSC analysis chart of g-C_3N_4. The TG and DSC diagrams of g-C_3N_4 could clearly reflect the following phase transition processes: When the temperature was raised from 0 to 609 °C, g-C_3N_4 absorbed heat slowly, while the TG data showed that the quality did not significantly change at this stage. This was because the melting point of g-C_3N_4 prepared in this work was about 609 °C, which was produced by endothermic melting. When the temperature was raised from 609 to 761 °C, the mass percentage of g-C_3N_4 sharply dropped, and the loss amount reached 92.07%. There was a strong exothermic peak at about 724 °C. This was because the temperature was too high, g-C_3N_4 was completely decomposed or sublimated, and the mass percentage at this time was zero.
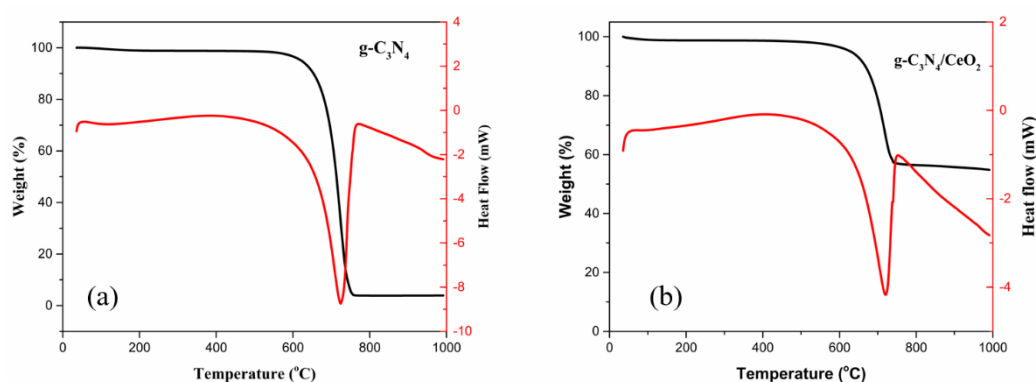

Figure 8. TG-DSC analysis of (**a**) g-C_3N_4 and (**b**) g-C_3N_4/CeO_2.

Figure 8b shows a TG-DSC analysis chart of g-C_3N_4/CeO_2. The TG and DSC diagrams of g-C_3N_4/CeO_2 clearly reflect the following phase transition processes: From 0 to 609 °C, g-C_3N_4/CeO_2 slowly absorbed heat, and the TG data showed that the quality did not significantly change at this stage. This was because the melting points of g-C_3N_4 and CeO_2 were about 609 and 2400 °C. g-C_3N_4 was melted endothermically. When the temperature was raised from 609 to 761 °C, the mass percentage sharply dropped, and the mass loss reached 42.86%. There was a strong exothermic peak around

753 °C as well. This was because the temperature was too high, $g-C_3N_4$ was completely decomposed or sublimated, and the mass percentage at this time was 57.14%. It can be speculated that the remaining material was CeO_2. It could be found from the mass loss percentage that the mixing mass ratio of $g-C_3N_4$ to CeO_2 was 0.75. The right shift of the exothermic peak of the $g-C_3N_4/CeO_2$ composite also showed that the two materials were connected together in the form of covalent bonds.

3.3.5. SEM

Figure 9 is the SEM images of $g-C_3N4$ [33], CeO_2, and $g-C_3N4/CeO_2$. As can be seen from the Figure 9a,b, $g-C_3N4$ is granular and porous, and CeO_2 is a rod-like structure. Figure 9c is the SEM image of $g-C_3N4/CeO_2$. It can be clearly seen from Figure 9 that layered $g-C_3N_4$ was attached to CeO_2. This fully and directly shows that $g-C_3N_4/CeO_2$ is a result of mutual doping.

(a)

(b)

(c)

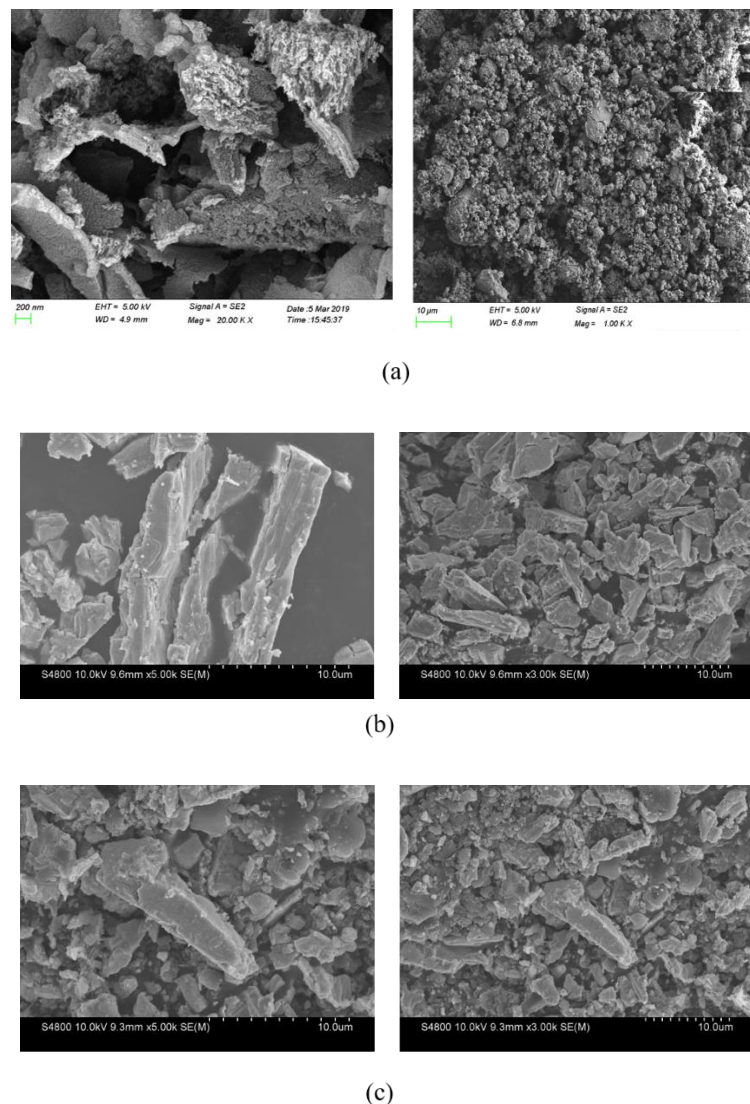**Figure 9.** SEM images of (**a**) $g-C_3N_4$, (**b**) CeO_2 and (**c**) $g-C_3N_4/CeO_2$.

3.3.6. XPS

Figure 10 is the XPS spectrum of $g-C_3N_4$. As can be seen from Figure 10a, the sample contained three elements of C, N, and O. The O element may have been caused by the sample not being dried or the surface having H_2O molecules. Figure 10b is the C 1s spectrum of $g-C_3N_4$. It can be seen from the figure that the peaks appeared at the binding energies of 284.8, 288.3, and 293.7 eV, which corresponded

to the C=C bond in the graphite phase carbon nitride and the NC=N and C–NH$_2$ bonds in the aromatic structure. Figure 10c is the N 1s spectrum of g-C$_3$N$_4$. It can be seen from the figure that peaks appeared at the binding energies of 398.7, 400.1, and 401.2 eV, respectively, corresponding to the CN = C bond in the triazine ring structure.

Figure 11 is the XPS spectrum of g-C$_3$N$_4$/CeO$_2$. Figure 11a is the full scan spectrum of the g-C$_3$N$_4$/CeO$_2$ sample. It can be seen from the figure that only C, N, Ce and O were detected in the g-C$_3$N$_4$/CeO$_2$ binary composite material. The prepared heterojunction composite was very pure, without other impurities. Figure 11b is the C 1s spectrum of the g-C$_3$N$_4$/CeO$_2$ sample. It can be seen from the figure that the peaks appeared at the binding energies of 284.9, 286.2, and 287.4 eV, which corresponded to the C–C, C–NH$_2$, and N=C–N$_2$ bonds in the s-triazine ring, respectively. Figure 11c is the N 1s spectrum of the g-C$_3$N$_4$/CeO$_2$ sample. It can be seen from the figure that the binding energy appeared peaks at 398.3, 400.2 and 401.8 eV. Among them, the main peak at the binding energy of 398.3 eV was an sp^2 heterocyclic nitrogen atom in the C=N bond. The peak at a binding energy of 400.2 eV corresponded to the nitrogen atom in the N–(C)$_3$ group. The corresponding peak at 401.8 eV was the nitrogen atom in the -NH$_2$ bond. Figure 11d is the O 1s spectrum of the g-C$_3$N$_4$/CeO$_2$ sample. It can be seen from the figure that the binding energy peaks appeared at 523.6 and 530.5 eV, which corresponded to the OH bond in the surface-attached water and Ce–O bond, respectively. Figure 11e is the Ce 3d spectrum of the g-C$_3$N$_4$/CeO$_2$ sample. It can be seen from the figure that there were many peaks of Ce element. Through the analysis of the Gaussian–Lorentzian function, it is possible to conclude that the characteristic peaks of Ce^{4+} 3d$^{5/2}$ and 3d$^{3/2}$ were located at the binding energies of 883.5 and 902.5 eV. Moreover, the characteristic peaks of Ce^{3+} 3d$^{5/2}$ and 3d$^{3/2}$ were located at the binding energies of 891.5 and 910.3 eV. This indicated that Ce element mainly existed in the trivalent and tetravalent states in the material.
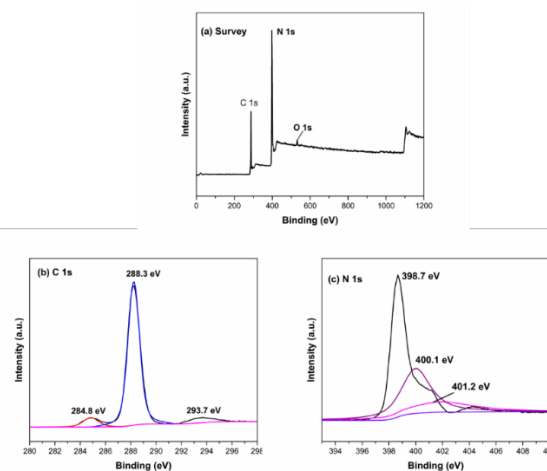

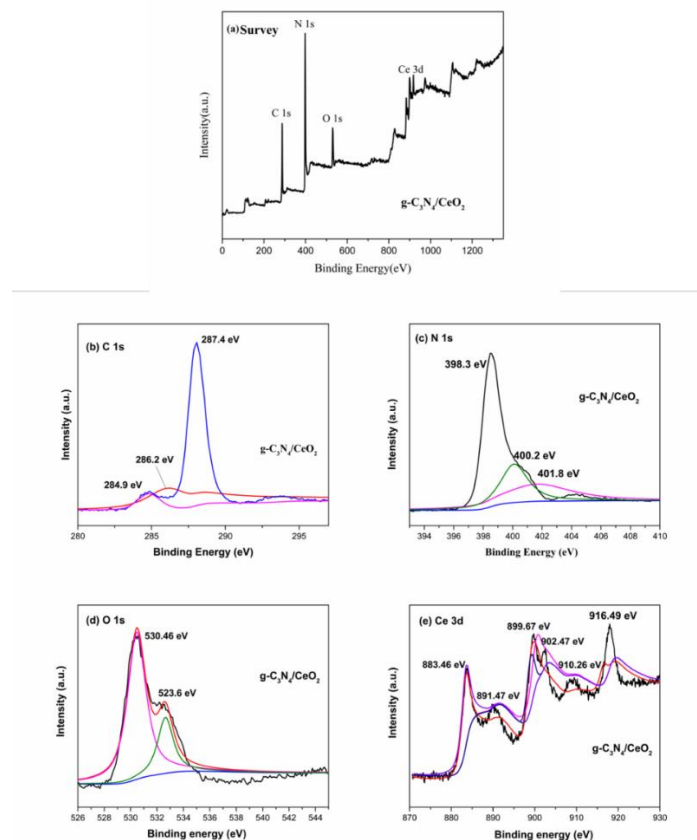**Figure 10.** XPS spectrum of g-C$_3$N$_4$: (**a**) survey, (**b**) C 1s and (**c**) N 1s.

Figure 11. XPS spectrum of g-C$_3$N$_4$/CeO$_2$: (**a**) survey, (**b**) C 1s, (**c**) N 1s, (**d**) O 1s and (**e**) Ce 3d.

4. Conclusions

The main content of this work is that a g-C$_3$N$_4$/CeO$_2$ heterostructure nanocomposite was prepared. The best mass ratio preparation of g-C$_3$N$_4$/CeO$_2$ was obtained by indoor exhaust gas degradation. The degradation efficiency for HC, CO, CO$_2$ and NO$_X$ were obtained under natural and ultraviolet light irradiation. Moreover, XRD, FI-IR, UV-Vis, TG-DSC, SEM, and XPS were conducted to investigate the morphology and structure of g-C$_3$N$_4$/CeO$_2$ heterostructure binary composite. The main conclusions are as follows:

(a) The exhaust gas purification efficiency of the g-C$_3$N$_4$/CeO$_2$ composite under natural light irradiation was higher than that under ultraviolet light. The best mass ratio preparation of g-C$_3$N$_4$/CeO$_2$ was 0.75.

(b) The degradation efficiencies of the g-C$_3$N$_4$/CeO$_2$ composite for HC, CO, CO$_2$ and NO$_X$ in 60 min were 7.59%, 12.10%, 8.25% and 36.82%, respectively. Under natural light irradiation, the degradation efficiencies for HC, CO, CO$_2$ and NO$_X$ in the 60 min were 15.88%, 16.22%, 10.45% and 40.58%, respectively.

(c) The microstructure characterized the crystal structure and micro-morphology of g-C$_3$N$_4$/CeO$_2$ composite. This indicated that g-C$_3$N$_4$/CeO$_2$ heterostructure nanocomposite was successfully prepared.

Conflicts of Interest: The authors declare that they have no known competing financial interests or personal relationships that could have appeared to influence the work reported in this paper.

References

1. Dong, F.; Sun, Y.J.; Zhang, Y.X. *Micro-Nano Structure Regulation of Graphite Phase C3N4 and Application of Photocatalytic Environmental Purification*, 1st ed.; Science Press: Beijing, China, 2018.

2. Smith, T.W.; Axon, C.J.; Darton, R.C. The impact on human health of car-related air pollution in the UK, 1995–2005. *Atmos. Environ.* **2013**, *77*, 260–266. [CrossRef]

3. Dong, P.Y.; Xi, X.G. *Visible Light-Responsive Photocatalytic Material*, 2nd ed.; Science Press: Beijing, China, 2017.

4. Fujishima, A.; Honda, K. Electrochemical Photolysis of Water at a Semiconductor Electrode. *Nature* **1972**, *238*, 37–38. [CrossRef] [PubMed]

5. Liu, B.S.; Zhao, X.J. *Heterogeneous Photocatalysis in Semiconductors: Research and Experimental Demonstration of Thermodynamic Mechanism*, 1st ed.; Science Press: Beijing, China, 2013.

6. Cui, S.C.; Li, R.; Ma, W.S.; Li, M.M.; Cui, J.X.; Pei, J.Z. Preparation, photocatalytic properties investigation and degradation rate study on nano-TiO_2 aerogels doped with Fe^{3+} for automobile emission purification. *Mater. Res. Express* **2018**, *5*, 115513. [CrossRef]

7. Chen, Y.F.; Tang, X.N.; Zhang, B.; Luo, Y.; Li, Y. $TiO_2@SiO_2$ Composites: Preparation and Photocatalytic Antimicrobial Performance. *J. Inorg. Mater.* **2019**, *34*, 1325–1333. [CrossRef]

8. Ton, N.Q.T.; Le, T.N.T.; Kim, S.; Dao, V.A.; Yi, J.; Vu, T.H.T. High-Efficiency Photo-Generated Charges of ZnO/TiO_2 Heterojunction Thin Films for Photocatalytic and Antibacterial Performance. *J. Nanosci. Nanotechnol.* **2020**, *20*, 2214–2222. [CrossRef] [PubMed]

9. Miao, Z.M.; Wang, G.L.; Li, L.J.; Wang, C.; Zhang, X.F. Fabrication of black TiO_2/TiO_2 homojunction for enhanced photocatalytic degradation. *J. Mater. Sci.* **2019**, *54*, 14320–14329. [CrossRef]

10. Tao, W.; Wang, M.K.; Ali, R. Multi-layered porous hierarchical $TiO_2/g-C_3N_4$ hybrid coating for enhanced visible light photocatalysis. *Appl. Surf. Sci.* **2019**, *495*, 143435. [CrossRef]

11. Haga, Y.; An, H.; Yosomiya, R. Photoconductive properties of TiO_2 films prepared by the sol–gel method and its application. *J. Mater. Sci.* **1997**, *32*, 3183–3188. [CrossRef]

12. Zhang, Y.H.; Gong, M.D.; Liu, X.; Ji, L.J.; Yang, Z.L.; Zhu, X.S. Preparation of activated carbon nanotube foams loaded with Ag-doped TiO_2 for highly efficient photocatalytic degradation under UV and visible light. *J. Mater. Sci.* **2019**, *54*, 975–2989. [CrossRef]

13. Ma, L.P.; Gu, Y.S.; Duan, Z.J.; Yuan, L.; Pang, S.J. Scanning tunneling microscopy investigation of carbon nitride thin films grown by microwave plasma chemical vapor deposition. *Thin Solid Films* **1999**, *349*, 10–13. [CrossRef]

14. Montigaud, H.; Tanguy, B.; Demazeau, G.; Alves, I.; Courjault, S. C_3N_4: Dream or reality? Solvothermal synthesis as macroscopic samples of the C_3N_4 graphitic form. *J. Mater. Sci.* **2000**, *35*, 2547–2552. [CrossRef]

15. Guo, Q.X.; Xie, Y.; Wang, X.J.; Lv, S.C.; Hou, T.; Liu, X.M. Characterization of well-crystallized graphitic carbon nitride nanocrystallites via a benzene-thermal route at low temperatures. *Chem. Phys. Lett.* **2003**, *308*, 84–87. [CrossRef]

16. Wang, X.C.; Maeda, K.; Thomas, A.; Takanabe, K.; Xin, G.; Carlsson, J.M.; Domen, K.; Antonietti, M. A metal-free polymeric photocatalyst for hydrogen production from water under visible light. *Nat. Mater.* **2009**, *8*, 76–80. [CrossRef] [PubMed]

17. Naseri, A.; Samadi, M.; Pourjavadi, A.; Moshfegh, A.Z.; Ramakrishna, S. Graphitic carbon nitride $(g-C_3N_4)$-based photocatalysts for solar hydrogen generation: Recent advances and future development directions. *J. Mater. Chem. A* **2017**, *5*, 23406–23433. [CrossRef]

18. Sun, S.D.; Gou, X.F.; Tao, S.S.; Cui, J.; Li, J.; Yang, Q.; Liang, S.H.; Yang, Z.M. Mesoporous graphitic carbon nitride $(g-C_3N_4)$ nanosheets synthesized from carbonated beverage-reformed commercial melamine for enhanced photocatalytic hydrogen evolution. *Mater. Chem. Front.* **2019**, *3*, 597–605. [CrossRef]

19. Jourshabani, M.; Shariatinia, Z.; Badiei, A. In situ fabrication of SnO_2/S-doped g-C_3N_4 nanocomposites and improved visible light driven photodegradation of methylene blue. *J. Mol. Liq.* **2017**, *248*, 688–702. [CrossRef]

20. Jia, J.K.; Jiang, C.Y.; Zhang, X.R.; Li, P.J.; Xiong, J.X.; Zhang, Z.; Wu, T.; Wang, Y.P. Urea-modified carbon quantum dots as electron mediator decorated g-C_3N_4/WO_3 with enhanced visible-light photocatalytic activity and mechanism insight. *Appl. Surf. Sci.* **2019**, *498*, 143524. [CrossRef]

21. Tu, X.M.; Zhou, R.T.; Guo, H.L.; Tao, W.Y. Heterojunction semiconductor g-C_3N_4/$BiVO_4$ with an enhanced photocatalytic activity based on the effective chemical bonding. *J. Mater. Technol.* **2019**, *34*, 827–837. [CrossRef]

22. Yan, H.; Zhu, Z.W.; Long, Y.M.; Li, W.F. Single-source-precursor-assisted synthesis of porous WO_3/g-C_3N_4 with enhanced photocatalytic property. *J. Colloid Surf. A* **2019**, *582*, 123857. [CrossRef]

23. Li, T. Preparation and Electrochemical Performance of Cerium Oxide-Based Composites. Master's Thesis, Shaanxi University of Science and Technology, Xi'an, China, 30 May 2018.

24. He, L.Y.; Su, Y.M.; Jiang, L.H.; Shi, S.K. Recent advances of cerium oxide nanoparticles in synthesis. luminescence and biomedical studies: A review. *J. Rare Earth* **2015**, *33*, 791–799. [CrossRef]

25. Xie, X.W.; Li, Y.; Liu, Z.Q.; Haruta, M.; Shen, W.J. Low-temperature oxidation of CO catalysed by Co_3O_4 nanorods. *Nature* **2009**, *7239*, 746–749. [CrossRef] [PubMed]

26. Wang, F.; Li, W.; Feng, X.L.; Liu, D.P.; Zhang, Y. Decoration of Pt on Cu/Co double-doped CeO_2 nanospheres and their greatly enhanced catalytic activity. *Chem. Sci.* **2016**, *7*, 1867–1873. [CrossRef] [PubMed]

27. Dey, S.; Dhal, G.C.; Mohan, D.; Prasad, R. Application of hopcalite catalyst for controlling carbon monoxide emission at cold-start emission conditions. *J. Traffic Transp. Eng.* **2019**, *6*, 419–440. [CrossRef]

28. Zhang, J.S.; Wang, B.; Wang, X.C. Carbon nitride polymeric semiconductor for photocatalysis. *Prog. Chem.* **2014**, *26*, 19–29.

29. Cui, S.C.; Li, R.; Zhu, C.D.; Pei, J.Z.; Wen, Y. Cerium-bismuth solid solution material prepared and application in automobile exhaust purification. *Sep. Purif. Technol.* **2020**, *239*, 116520. [CrossRef]

30. Yuan, X.Y.; Zhou, C.; Jin, Y.R.; Jing, Q.Y.; Yang, Y.L.; Shen, X.; Tang, Q.; Mu, Y.H.; Du, A.K. Facile synthesis of 3D porous thermally exfoliated g-C_3N_4 nanosheet with enhanced photocatalytic degradation of organic dye. *J. Colloid Interface Sci.* **2016**, *468*, 211–219. [CrossRef]

31. Makula, P.; Pacia, M.; Macyk, W. How to Correctly Determine the Band Gap Energy of Modified Semiconductor Photocatalysts Based on UV-Vis Spectra. *J. Phys. Chem. Lett.* **2018**, *9*, 6814–6817. [CrossRef]

32. Cui, P.P.; Hu, Y.; Zheng, M.M.; Wei, C.H. Enhancement of visible-light photocatalytic activities of $BiVO_4$ coupled with g-C_3N_4 prepared using different precursors. *Environ. Sci. Pollut. Res.* **2018**, *25*, 32466–32477. [CrossRef]

33. Cui, S.C.; Li, R.; Pei, J.Z.; Wen, Y.; Li, Y.; Xing, X.Y. Automobile exhaust purification over g-C_3N_4 catalyst material. *Mater. Chem. Phys.* **2020**, 112867.